Int. J. Therm. Sci. (2001) 40, 279–287

S1290-0729(00)01218-7/FLA

Heat transfer modeling at high temperature for the evaluation of atomic oxygen recombination energy on ceramic materials

Marianne Balat-Pichelin *, Florent Duqueroie

Institut de science et de génie des Matériaux et Procédés, IMP-CNRS, UPR 8521, BP 5, 66125 Odeillo, Font-Romeu cedex, France

(Received 1 October 1999, accepted 27 April 2000)

Abstract — The heat transfer modeling in ceramic materials at high temperature follows the experimental determination of the recombination thermal flux of atomic oxygen under air plasma conditions. The experimental study for the measurement of the atomic oxygen recombination energy on silicon- or aluminum-based ceramic materials, at high temperature (1 000–1 800 K) has been performed for different pressures (200–2 000 Pa) by a "thermal" understanding. This experimental evaluation is realized using some assumptions and in this paper, the present modeling leads to obtain more accurate results accounting for the lateral thermal losses at the sample edges and convection that we have previously ignored. So, the recombination fluxes obtained are higher than the experimental ones of fairly 12%. The temperature mapping of the hot surfaces of the samples obtained by the modeling using Matlab™ are compared to experimental infrared images. © 2001 Éditions scientifiques et médicales Elsevier SAS

modeling / heat transfer / microwave plasma / recombination / infrared image / high temperature

Nomenclature

A_i	coefficient of temperature at node i (equation (10))	
C_i	boundary conditions at the node i	
Cp	specific heat	$J \cdot kg^{-1} \cdot K^{-1}$
E	electric field	$V \cdot m^{-1}$
f	frequency	Hz
H	heat transfer coefficient	$W \cdot m^{-2} \cdot K^{-1}$
i	index of node	
Ir, Iz	coordinates along r, along z	m
Nr, Nz	node number along r, along z	
P	total pressure	Pa
q	heat flux	$W \cdot m^{-2}$
r	radial coordinate	m
RHS	temperature + boundary conditions matrix	
t	time	s
T	temperature	K
TC	temperature matrix	
z	axial coordinate	m

Greek letters

α	apparent solar absorptivity coefficient	
β	accomodation coefficient	
ε	total hemispherical emissivity	
κ	complex dielectric permittivity	
κ'	real part of κ, dielectric constant	
κ''	imaginary part of κ, dielectric loss factor	
λ	axial thermal conductivity	$W \cdot m^{-1} \cdot K^{-1}$
μ	radial thermal conductivity	$W \cdot m^{-1} \cdot K^{-1}$
ρ	density	$kg \cdot m^{-3}$
σ	Stefan–Boltzmann constant	$W \cdot K^{-4} \cdot m^{-2}$
δT	difference between two temperatures	K

Subscripts

ambc	ambient convection
ambr	ambient radiation
b	back face of the sample
em	electromagnetic (relative to the microwave–material interaction)
eff	effective
exp	experimental
f	front face of the sample
i	point
int	internal

* Correspondence and reprints.
E-mail address: balat@imp.cnrs.fr (M. Balat-Pichelin).

lat	lateral thermal losses at the limit of the reference cylinder
rad	radiative transfer
rec	recombination
sol	solar
1D	one-dimensional
2D	two-dimensional

Superscripts

air	under air flow
arg	under argon flow
n	time
*	under plasma conditions
1D	one-dimensional
2D	two-dimensional

1. INTRODUCTION

During the hypersonic trajectory of a spacecraft, the vehicle entering in a planet atmosphere creates a shock wave leading to very high temperatures. The created excited species (ions, atoms, molecules, electrons) diffuse in the boundary layer and react with the materials of the vehicle (nose cap, wind leading edges etc.). Atomic oxygen (major species) and nitrogen (or CO) present for terrestrial (or martian) entries can strike the surface of the vehicle and recombine to form molecules so that they produce an increase of the surface temperature and can affect the integrity of the material.

The purpose of this paper is to present a heat transfer modeling for the evaluation of the atomic oxygen recombination energy on ceramic materials, which can be used as protective thermal shield in a spacecraft, at high temperature. The aim is to obtain the less catalytic ceramic material towards atomic oxygen recombination. A comparison is done between:

- the experimental values of the thermal recombination flux and the values obtained by modeling;
- the temperature mapping of the samples obtained by modeling and those experimentally acquired using an infrared camera.

2. EXPERIMENTAL RECOMBINATION FLUX EVALUATION

The recombination thermal flux is obtained using a method developed in our laboratory for terrestrial (air) or martian (CO_2) entries using an hybrid heating experimental set-up called MESOX (*Moyen d'Essai Solaire d'Oxydation*) which associates a solar radiation concentrator (for high temperatures) to a microwave generator (for dissociated species) [1].

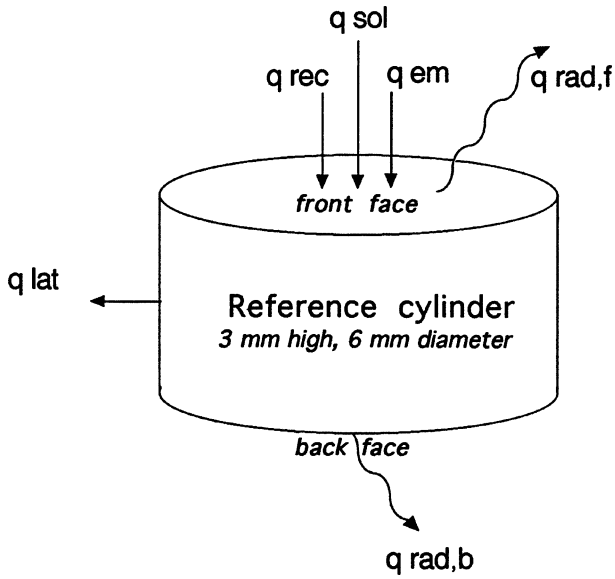

Figure 1. Representation of the different fluxes on the reference cylinder chosen in the sample volume heated by solar radiation under microwave-induced air plasma.

The thermal approach developed for molecular and/or atomic species recombination uses a heat balance over a reference cylindrical volume (6 mm in diameter, 3 mm in height) comprised in the sample volume (25 mm in diameter, 3 mm in height) (*figure 1*). The area of this cylindrical part of the sample, considered for the thermal balance, represents the measurement area by pyrometry. The equations for steady state heat transfer under different environments are written neglecting convective phenomena compared to the radiative fluxes.

The thermal balance is established under four atmospheres: standard reactive gas (air or CO_2), reactive gas plasma, standard nonreactive gas (argon) and nonreactive argon plasma, for the experimental verification of some assumptions. Then, the determination of the recombination flux is done by measuring the difference between the experiments under reactive gas plasma (air or CO_2) and inert gas plasma (argon). In the case of an air microwave-excited atmosphere, the recombination flux is determined by

$$\beta q_{\mathrm{rec}} = q_{\mathrm{rad,f}}^{\mathrm{air}} - q_{\mathrm{rad,f}}^{\mathrm{arg}} + q_{\mathrm{rad,b}}^{\mathrm{air}} - q_{\mathrm{rad,b}}^{\mathrm{arg}} + q_{\mathrm{em}}^{\mathrm{air}} - q_{\mathrm{em}}^{\mathrm{arg}} + q_{\mathrm{lat}}^{\mathrm{air}} - q_{\mathrm{lat}}^{\mathrm{arg}} \quad (1)$$

β being the accomodation coefficient, q_{rec} the recombination thermal flux, $q_{\mathrm{rad,f}}$ and $q_{\mathrm{rad,b}}$ respectively the ra-

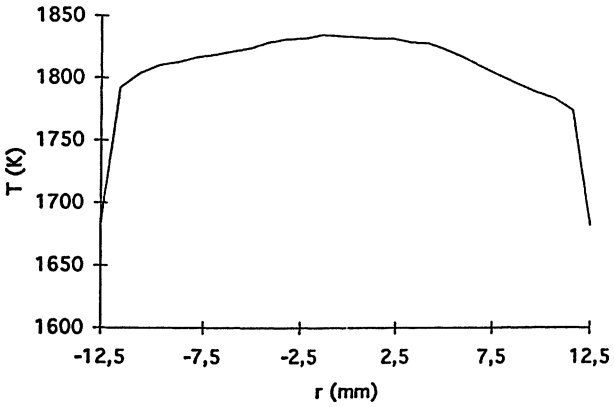

Figure 2. Experimental temperature profile of the front face of a SiC sample under microwave air plasma obtained by infrared camera.

diative fluxes on the sample front face f and on the sample back face b, q_{em} the microwave power dissipation in the sample, and q_{lat} the radial losses by conduction at the limit of the reference cylindrical volume. Superscripts ^{air} and ^{arg} refer to the gas nature.

The following assumptions (some are verified by experimental measurements) are made:

- without plasma, the same temperature level is reached both for air and argon atmospheres, that is $T_f^{air} = T_f^{arg}$ and $T_b^{air} = T_b^{arg}$; this is obtained thanks to the constant solar flux, experiments being performed around the period of solar zenith;
- under plasma conditions, the microwave–material interactions for both atmospheres are supposed like equal so that $q_{em}^{air} = q_{em}^{arg}$;
- the absorbed solar energy is constant under the different atmospheres for a given shutter opening because during all the experiment the incident solar flux is constant;
- the difference between the radial losses by conduction (under air and argon plasmas) out of the reference cylinder is neglected.

Infrared imaging on the front face of the sample has allowed us to determine a very low radial temperature gradient (nearly 10 K) as a function of distance from the centre, even when the sample is heated under air or argon plasma (*figure 2*). So, this approximation is equivalent to a one-dimensional hypothesis and equation (1) reduces to

$$\beta q_{rec}^{air} = q_{rad,f}^{air} - q_{rad,f}^{arg} + q_{rad,b}^{air} - q_{rad,b}^{arg} \qquad (2)$$

equivalent to

$$\beta q_{rec}^{air} = \varepsilon\sigma\left[\left(T_f^{air}\right)^4 - \left(T_f^{arg}\right)^4 + \left(T_b^{air}\right)^4 - \left(T_b^{arg}\right)^4\right] \quad (3)$$

with ε the total hemispherical emissivity, σ the Stefan–Boltzman constant, T_f and T_b respectively the sample front face f and the sample back face b temperatures.

The absorbed recombination flux can be calculated from the following parameters: ε the total hemispherical emissivity (measured in our laboratory by a direct method) and the front and back face temperatures under air and argon plasmas.

3. HEAT TRANSFER MODELING

A 2D model is developed in order to estimate the radial thermal losses which have been neglected in equation (2), on the whole sample, and to calculate by parameter identification the recombination thermal flux. This model is based on the simulation of axial and radial heat transfers in the material at high temperature. The two-direction heat equation with added source terms (one due to the microwave–material interaction, since the sample is in the electromagnetic field and another one due to the recombination) is solved with a finite difference scheme which is applied to a cylindrical shape. This code is written with Matlab^{TM} and gives a temperature mapping of the sample front face (where recombination occurs) which is compared to camera-obtained infrared images. The code gives also the sample back face temperature mapping and that of its thickness.

3.1. Microwave–material interaction

In the experimental configuration for the evaluation of the recombination flux, the sample is located in the microwave discharge zone. So, there exists an interaction between the electromagnetic field emitted at 2.45 GHz and the ceramic sample, leading to a volumetric heat source coming from the centre of the sample [2–12]. In this way, a volumetric power q_{em} is absorbed by the nonmagnetic material according to the relation

$$q_{em} = 2\pi f \kappa'' E_{int}^2 \qquad (4)$$

with f the frequency of the electric field, κ'' the imaginary part (dielectric loss factor) of the complex permittivity κ ($\kappa = \kappa' - j\kappa''$) of the material and E_{int} the electric field through the material. The electric field geometry can be entirely defined by Maxwell's equations if the electromagnetic properties of the material and the field created in the wave guide (boundary conditions) are known.

The complex permittivity κ of the material depends upon temperature, shape, grain size, porosity, density, impurities, defects etc. and microwave frequency [4, 6, 8–14].

The first problem is the knowledge of the characteristics of the microwave field passing through the sample. The second one is the determination of the dielectric loss factor according to the composition of the sample and its temperature.

For the electromagnetic field, many authors consider that in a thin sample highly transparent to microwaves like ceramic materials such as Al_2O_3, SiO_2 etc., the assumption of a constant electromagnetic field is reasonable [3, 9, 10, 12].

A great amount of dielectric property data for oxides, carbides etc. has been measured and compiled by Westphal and Sils [15]. Even though large variations are encountered in the values of dielectric constants and losses for ceramic materials, the loss factor globally increases with temperature for many of them [6, 10, 15, 16]. In the case of alumina, Spotz et al. [10] give different results for the dielectric loss factor (κ'') and for the dielectric constant (κ') according to its purity, and the evolution of these parameters is very sensitive to temperature. When the temperature and the amount of impurities increase, the dielectric permittivity increases very quickly.

The induced thermal runaway is presented by many authors [3, 4, 6, 7, 9, 12, 14, 17, 18] but in our case, the thermal runaway does not occur due to the hybrid heating as also observed by Spotz et al. [10]. Hybrid heating (solar concentrated radiation and microwave) reduces the temperature gradients in the sample as one mode of heating alone. Moreover, these two modes of heating are complementary, one coming on the surface (solar concentrated radiation) and the other one from the centre of the sample (microwave); the opposite directions of the flux result in small temperature gradients within the sample. Generally, the temperature gradient between the sample core and its surface during microwave heating is attributable to thermal losses at the sample surface which occur due to imperfect insulation around the sample. But in our experiment, this is counter-balanced by the thermal solar source arriving on the surface.

3.2. Modeling

In our experiment, the samples are small and the depth of the microwave penetration (several cm) is larger than the characteristics of the sample dimension. So, the internal electric field E_{int} is supposed to be homogeneous in the whole sample more especially as the wavelength is constant.

Some authors [2, 5, 11, 13] have chosen to take into account the amount of the absorbed power due to the microwave–material interaction as an added source term in the heat equation as we have done. For Chen and Chen [2], the effect of the microwave energy loss in the sample is represented using an unknown equivalent internal heat source and the resolution of an inverse source problem of the nonlinear diffusion equation from the surface temperature is done to finally determine this unknown internal heat source.

We have chosen to take into account the thermal contribution of the microwaves in the material and then modeled by an added source term q_{em}, depending only on temperature in the classical heat equation as

$$\rho Cp\frac{\partial T}{\partial t} = \nabla(\lambda\nabla T) + q_{\text{em}}(T) + q_{\text{rec}}(T) \tag{5}$$

with ρ the material density, Cp the specific heat, T the temperature, t the time, λ the thermal conductivity and q_{rec} an additional source term due to the exothermic contribution of the recombination of atomic oxygen. We use a 2D anisotropic model, with a cylindrical geometry, so equation (5) is written as

$$\rho Cp\frac{\partial T}{\partial t} = \lambda\frac{\partial^2 T}{\partial z^2} + \frac{\partial\lambda}{\partial z}\frac{\partial T}{\partial z} + \mu\frac{\partial^2 T}{\partial r^2} + \frac{\partial\mu}{\partial r}\frac{\partial T}{\partial r} + \frac{\mu}{r}\frac{\partial T}{\partial r} + q_{\text{em}}(T) + q_{\text{rec}}(T) \tag{6}$$

with z the axial coordinate, λ the axial thermal conductivity, r the radial coordinate and μ the radial thermal conductivity. This thermal conductivity divided in λ and μ is useful for composite materials like C/SiC which are highly anisotropic.

The boundary conditions on respectively the front, back and lateral walls of the sample are the following:

- front face:

$$\lambda\frac{\partial T}{\partial z} = q_{\text{f}} = \alpha q_{\text{sol}} - H(T - T_{\text{ambc}}) - \varepsilon\sigma\left(T^4 - T_{\text{ambr}}^4\right) \tag{7}$$

- back face:

$$\lambda\frac{\partial T}{\partial z} = q_{\text{b}} = H(T - T_{\text{ambc}}) + \varepsilon\sigma\left(T^4 - T_{\text{ambr}}^4\right) \tag{8}$$

- lateral wall:

$$\mu\frac{\partial T}{\partial t} = q_{\text{lat}} = -H(T - T_{\text{ambc}}) - \varepsilon\sigma\left(T^4 - T_{\text{ambr}}^4\right) \tag{9}$$

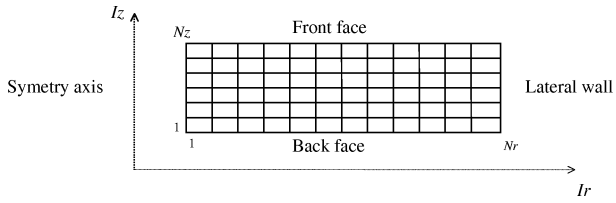

Figure 3. Mesh grid (25 × 6 nodes) for the half sample.

with α the apparent solar absorptivity, q_{sol} the incident solar flux, H the convective heat transfer coefficient, T_{ambc} the ambient temperature of convection, T_{ambr} the ambient temperature of radiation, ε the total hemispherical emissivity and σ the Stefan–Boltzmann constant.

The temperature distribution is symetrical with regards to the cylinder axis (z), so for the modeling, we use only a section along a perpendicular plane to the cylinder basis and containing the axis (*figure 3*). The chosen method is that of finite difference. The theoretical study and the discretization calculation were done by Ferriere et al. [19]. For the numbering of each node, we use a unique index: at the node of (Iz, Ir) coordinates corresponds the index $i = Iz + (Ir - 1)Nz$.

After the discretization problem, for each node i, the following equation is established:

$$T_i^{n-1} + C_i = A_0 T_i^n + A_1 T_{i+Nz}^n + A_2 T_{i-Nz}^n + A_3 T_{i+1}^n + A_4 T_{i-1}^n \qquad (10)$$

with T_i^n the temperature at the point i at the time n.

The quantity C_i includes the boundary conditions at the node i and the sources terms $q_{\mathrm{em}}(T)$ and $q_{\mathrm{rec}}(T)$ when it is necessary.

Finally, the problem consists in solving the linear system:

$$RHS = A\,TC$$

with

$$TC = \begin{pmatrix} T_1^n \\ \vdots \\ T_{Nz\times Nr}^n \end{pmatrix} \quad \text{and} \quad RHS = \begin{pmatrix} T_1^{n-1} + C_1 \\ \vdots \\ T_{Nz\times Nr}^{n-1} + C_{Nz\times Nr} \end{pmatrix}$$

The problem is solved by using the codes called MAT2D and REC2D. With the material characteristics and the boundary conditions, the codes compute the temperature distribution in the sample (MAT2D) and determine the recombination heat flux $q_{\mathrm{rec}}^{2\mathrm{D}}$ (REC2D) which is compared to the experimental value $q_{\mathrm{rec}}^{1\mathrm{D}}$.

3.3. Algorithm of the modeling for the determination of $q_{\mathrm{rec}}^{\mathbf{2D}}$

For the determination of the recombination heat flux using the code REC2D, several stages are necessary. At each stage, one parameter is identified according to the experimental values of temperature. This parameter is validated when the computed temperatures are equal to the experimental ones. The different stages are the following:

- First, an experiment is done under standard air. The microwave flux absorbed by the sample and the recombination flux are equal to zero. In this case, the value of the incident solar flux q_{sol} is measured using a calorimeter. The only unknown value is the apparent solar absorptivity α. Its value is assumed to be correct when $T_{2\mathrm{D}}^{\mathrm{air}} = T_{\mathrm{exp}}^{\mathrm{air}}$, that is to say when the temperatures obtained by the modeling and the experiment are equal.
- Second, an experiment is performed under argon plasma. The recombination heat flux is equal to zero. The apparent solar absorptivity is known by the first stage, so the only unknown is, in this case, the microwave flux absorbed by the sample. As previously, its value is supposed to be correct when $T_{2\mathrm{D}}^{\mathrm{arg}^*} = T_{\mathrm{exp}}^{\mathrm{arg}^*}$ under plasma conditions (*).
- The last stage is an experiment under air plasma (reactive gas). The apparent solar absorptivity α and the microwave flux absorbed by the sample q_{em} are known using the preceding stages, so the only unknown is now the recombination heat flux transferred to the surface sample βq_{rec}. Its value is determined when $T_{2\mathrm{D}}^{\mathrm{air}^*} = T_{\mathrm{exp}}^{\mathrm{air}^*}$ under air plasma conditions ($^{\mathrm{air}^*}$).

The algorithm is presented in *figure 4*.

3.4. Comparison of modeling and experimental results

The calculations are done for different materials (SiC, composite C/SiC, $SiC + SiO_2$, Si_3N_4, AlN and Al_2O_3 in several forms: sintered, foam and coating on AlN). We only present here the results obtained with some sintered materials (SiC, Si_3N_4, AlN and Al_2O_3) whose morphological and chemical properties are given in *table I*. The different characteristics of the materials are fixed according to:

- the total hemispherical emissivity of the sample is measured in our laboratory using a direct method (*table I*);

TABLE I
Ceramic material characteristics and properties used for the recombination thermal flux evaluation.

Materials	SiC	Si_3N_4	AlN	Al_2O_3
Reference manufacturer	SiC 100	SiN 220	AlN 300	AF 997
Sintering aids	B	O, Al, Y	Y_2O_3	–
Crystal structure	α 6H	β hexag.	hexagonal	α
Density: apparent/theor.	3.10/3.21	3.20/3.28	$\approx$ 3.30/3.30	3.85/3.98
Total porosity (% vol.)	0	< 0.5	< 2.0	0
Surface roughness (μm)	0.03	0.05	0.14	0.63
Total hemisph. emissivity	0.90 ± 0.01	0.90 ± 0.02	0.81 ± 0.01	0.40 ± 0.02

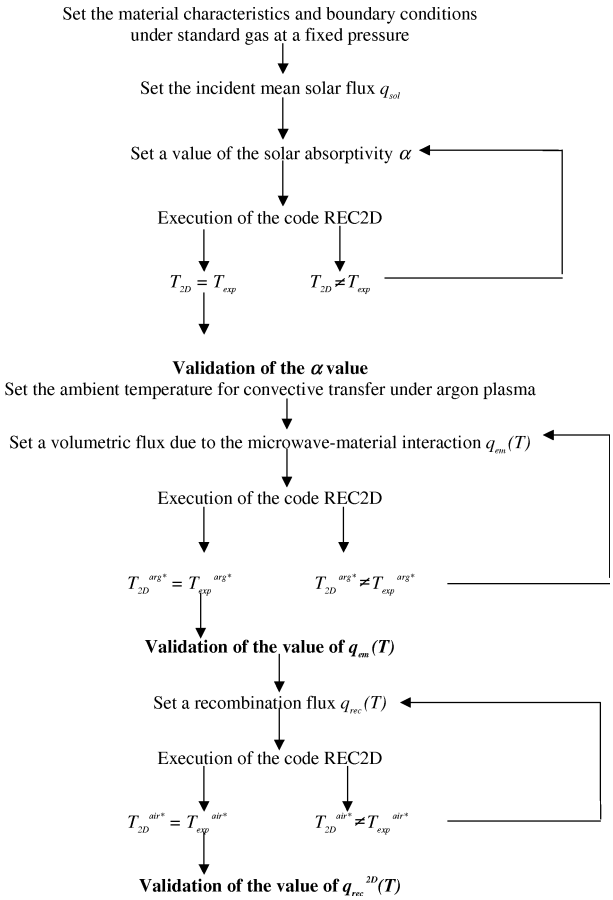

Figure 4. Algorithm for the identification of the recombination flux $q_{\mathrm{rec}}^{2\mathrm{D}}$.

• the thermal conductivities λ and for the composite μ are given by the sample manufacturer;

• the heat transfer coefficient H equals to 2 $\mathrm{W{\cdot}m^{-2}{\cdot}K^{-1}}$ for experiments conducted at 200 Pa total air pressure and to 5 $\mathrm{W{\cdot}m^{-2}{\cdot}K^{-1}}$ under 2 000 Pa. We have verified that the value of H has a very low influence on the final result;

• the ambient temperature corresponding to the convective transfer is fixed at 300 K under standard gas and to 800 K under air plasma conditions. The later value is the gas temperature we have measured in our laboratory using optical emission spectroscopy.

Nevertheless, we have to make some assumptions:

• the recombination flux is supposed uniform on the sample front face surface and equal to zero on the back face (the gas flow impinges the front face);

• the heat flux due to the absorption of the microwaves by the material is supposed equal under argon and air plasmas; it depends only on the material properties and temperature: $q_{\mathrm{em}}(T^{\mathrm{air}^*}) = q_{\mathrm{em}}(T^{\mathrm{arg}^*})$.

All the results compared with the experimental ones are given in *tables II–V*. Most results obtained by the model REC2D are in good agreement with the experimental values taking into account the accuracy of the experimental results. The results obtained for sintered SiC (less catalytic ceramic) and Al_2O_3 (highest catalytic ceramic) at 200 and 2 000 Pa air, under plasma conditions, are given in *tables II* and *V*. The recombination flux values obtained by experiment ($\beta q_{\mathrm{rec}}^{1\mathrm{D}}$) are very near the calculated one ($\beta q_{\mathrm{rec}}^{2\mathrm{D}}$), thus proving that the hypotheses chosen for the experimental evaluation are valid for all the ceramic materials tested. The main hypothesis (difference between both radial losses negligible) appears to be less important at high temperature as shown in *tables II–V*, so the experimental results present a better accuracy at high temperature (1 600–1 800 K).

Figure 5 presents the temperature increase ($\delta T^{\mathrm{arg}} = T^{\mathrm{arg}^*} - T^{\mathrm{arg}}$) induced by the microwave–material interaction for sintered SiC and Al_2O_3 versus surface temperature, and *figure 6* represents the identified microwave absorbed flux for the same materials, for a constant incident microwave power of 300 W (reflected power $\cong$ 0 W). For

TABLE II
Experimental data for atomic oxygen recombination on sintered SiC at 2 000 Pa and 200 Pa (front face temperature T_f, thermal recombination flux βq_{rec}, modeling: 2D and experimental: 1D).

2 000 Pa			200 Pa		
T_f [K]	βq_{rec}^{2D} [kW·m^{-2}]	βq_{rec}^{1D} [kW·m^{-2}]	T_f [K]	βq_{rec}^{2D} [kW·m^{-2}]	βq_{rec}^{1D} [kW·m^{-2}]
984 ± 3	43	37 ± 3	984 ± 3	34	30 ± 2
1 196 ± 5	40	35 ± 3	1 191 ± 5	31	29 ± 2
1 386 ± 7	38	33 ± 3	1 377 ± 7	32	30 ± 3
1 598 ± 9	36	34 ± 3	1 591 ± 9	26	25 ± 3
1 775 ± 11	40	36 ± 4	1 780 ± 11	15	13 ± 2

TABLE III
Experimental data for atomic oxygen recombination on sintered Si_3N_4 at 2 000 Pa and 200 Pa (front face temperature T_f, thermal recombination flux βq_{rec}, modeling: 2D and experimental: 1D).

2 000 Pa			200 Pa		
T_f [K]	βq_{rec}^{2D} [kW·m^{-2}]	βq_{rec}^{1D} [kW·m^{-2}]	T_f [K]	βq_{rec}^{2D} [kW·m^{-2}]	βq_{rec}^{1D} [kW·m^{-2}]
984 ± 3	64	58 ± 5	991 ± 3	50	46 ± 4
1 175 ± 4	55	51 ± 4	1 175 ± 4	50	46 ± 4
1 384 ± 6	54	51 ± 5	1 369 ± 6	35	32 ± 3
1 570 ± 8	36	32 ± 3	1 580 ± 8	31	29 ± 3
1 776 ± 10	45	39 ± 5	1 772 ± 10	43	45 ± 5

TABLE IV
Experimental data for atomic oxygen recombination on sintered AlN at 2 000 Pa and 200 Pa (front face temperature T_f, thermal recombination flux βq_{rec}, modeling: 2D and experimental: 1D).

2 000 Pa			200 Pa		
T_f [K]	βq_{rec}^{2D} [kW·m^{-2}]	βq_{rec}^{1D} [kW·m^{-2}]	T_f [K]	βq_{rec}^{2D} [kW·m^{-2}]	βq_{rec}^{1D} [kW·m^{-2}]
977 ± 3	85	71 ± 5	1 006 ± 4	64	56 ± 4
1 171 ± 4	78	67 ± 5	1 203 ± 5	65	58 ± 4
1 373 ± 6	80	70 ± 6	1 380 ± 6	52	46 ± 4
1 579 ± 9	56	50 ± 5	1 590 ± 9	49	43 ± 5
1 812 ± 11	67	61 ± 7	1 800 ± 11	63	63 ± 7

TABLE V
Experimental data for atomic oxygen recombination on sintered Al_2O_3 at 2 000 Pa and 200 Pa (front face temperature T_f thermal recombination flux βq_{rec}, modeling: 2D and experimental: 1D).

2 000 Pa			200 Pa		
T_f [K]	βq_{rec}^{2D} [kW·m^{-2}]	βq_{rec}^{1D} [kW·m^{-2}]	T_f [K]	βq_{rec}^{2D} [kW·m^{-2}]	βq_{rec}^{1D} [kW·m^{-2}]
982 ± 6	154	136 ± 22	975 ± 6	109	97 ± 16
1 173 ± 9	168	149 ± 27	1 168 ± 9	153	139 ± 24
1 364 ± 11	202	184 ± 37	1 399 ± 11	166	151 ± 29
1 597 ± 16	126	113 ± 25	1 577 ± 16	120	108 ± 23
1 767 ± 21	106	93 ± 23	1 710 ± 20	–	65 ± 16

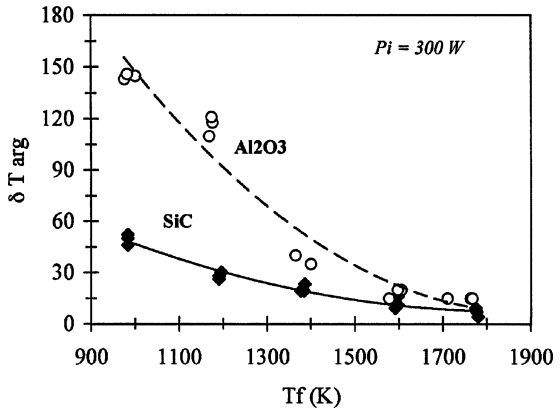

Figure 5. Temperature increase due to the microwave–material interaction versus front face temperature under argon plasma for sintered SiC and Al_2O_3. P_i is the incident microwave power.

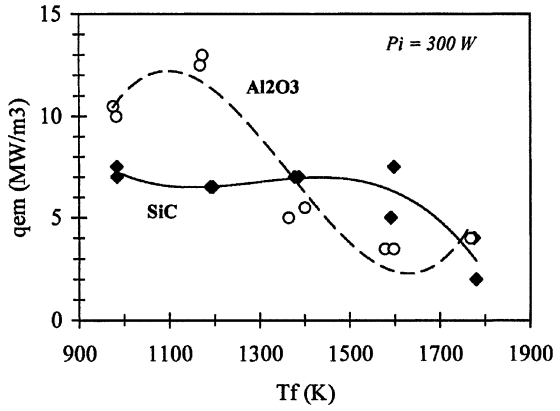

Figure 6. Calculated values of the volumetric absorbed power by the sample (q_{em}) versus front face temperature for sintered SiC and Al_2O_3. P_i is the incident microwave power.

SiC, the temperature increase due to the interaction with microwaves is not as important (50° at 1 000 K to 7° at 1 800 K) as in the case of Al_2O_3 (150° at 1 000 K to 15° at 1 800 K). This could be due to the different dielectric properties and thermal conductivities of these two materials. It would be necessary now to measure the dielectric constant and loss factor at 2.45 GHz at high temperature to confirm this evolution.

The identification of the absorbed power (*figure 6*) shows a strong temperature dependence for Al_2O_3. These variations with temperature can also be confirmed by performing dielectric property measurements at high temperature. The dielectric loss factors, at ambient temperature, of SiC (0.2) and Al_2O_3 (10^{-4}) are very different but it is necessary to know the evolution of this parameter with temperature. Westphal and Sils [15] have given several dielectric properties of different kinds of alumina with temperature and strong variations can be encountered with the same trend as those we have obtained for the microwave absorbed power.

3.5. Comparison with infrared images

Infrared images are obtained using an Agema Thermovision® 900 SW camera. *Figure 7* presents an example of the temperature mapping in the front surface sample (sintered SiC) obtained by modeling (code MAT2D, on the left) and those experimentally acquired (on the right) under air plasma conditions at a total pressure of 2 000 Pa. This figure shows that the experimental infrared images and the results of the modeling are in good agreement and this is also confirmed by the values obtained by the calculation of the recombination heat flux (*table II*). Nevertheless, it seems that this model does not correctly predict the values at the sample edges. We think that the presence of the sample holder and the knowledge of its temperature during the experiment are important in order to improve the boundary conditions which must be taken into account in the model.

4. CONCLUSION

The determination of the atomic oxygen recombination energy transferred at the surface of different ceramic materials under microwave air plasma at low pressure (200–2 000 Pa) has been realized in the MESOX set-up in the temperature range 1 000–1 800 K.

The first part of this study is focussed on the thermal balance of heat fluxes on a sample under air and argon plasmas and is established for several ceramic materials. This approach leads to the determination of the recombination heat fluxes according to a one-dimensional hypothesis. Catalytic behaviors for different materials change a little between 1 000 and 1 400 K, except for Al_2O_3 for which recombination fluxes vary strongly and reach a maximum at 1 400 K. Most of the studied materials are weakly catalytic (except Al_2O_3) and are classified according to a catalytic scale available between 1 000 and 1 800 K: $SiC < Si_3N_4 < AlN \ll Al_2O_3$.

The second part presents a heat transfer modeling at high temperature which has been developed in order

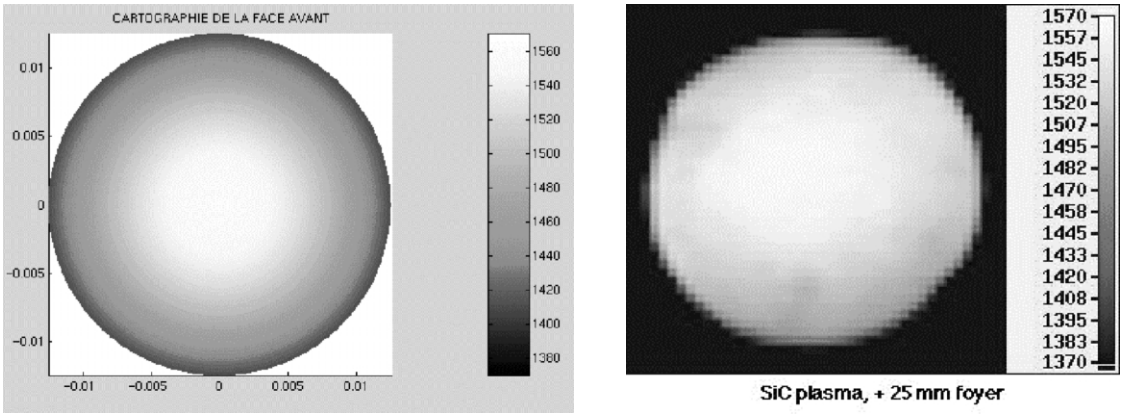

Figure 7. Comparison of the front face temperature mapping of a sintered SiC sample under air plasma: on the left, modeling and on the right, infrared image. The temperatures are in °C.

to identify the absorbed microwave flux and finally the recombination heat flux and, also, to precise the validity of the experimental assumptions. The catalytic scale is confirmed by using the two-dimensional modeling and give more accurate values of recombination fluxes particularly for temperatures lower than 1 400 K; the discrepancy between modeling and experimental values of the recombination thermal flux being less important at higher temperature levels (1 600–1 800 K).

REFERENCES

[1] Balat M., Czerniak M., Badie J.M., Thermal and chemical approaches for oxygen catalytic recombination evaluation on ceramic materials at high temperature, Appl. Surf. Sci. 120 (1997) 225–238.

[2] Chen X., Chen Y.M., Efficient algorithm for solving inverse source problems of a nonlinear diffusion equation in microwave heating, J. Comput. Phys. 132 (1997) 374–383.

[3] Kenkre V.M., Theory of microwave interactions with ceramic materials, Ceram. Trans. 21 (1991) 69–80.

[4] Kenkre V.M., Skala L., Weiser M.W., Katz J.D., Theory of microwave interactions in ceramic materials: the phenomenon of thermal runaway, J. Mat. Sci. 26 (1991) 2483–2489.

[5] Lagos L.E., Li W., Ebadian M.A., White T.L., Grubb R.G., Foster D., Heat transfer within a concrete slab with a finite microwave heating source, Int. J. Heat Mass Tran. 38 (5) (1995) 887–897.

[6] Martin L.P., Dadon D., Rosen M., Gershon D., Rybakov K.I., Birman A., Calame J.P., Levush B., Carmel Y., Hutcheon R., Effects of anomalous permittivity on the microwave heating of zinc oxide, J. Appl. Phys. 83 (1998) 432–437.

[7] Parris P.E., Kenkre V.M., Thermal runaway in ceramics arising from the temperature dependence of the thermal conductivity, Phys. Stat. Solidi B 200 (1997) 39–47.

[8] Penn S.J., Alford N.N., Templeton A., Wang X., Xu M., Reece M., Schrapel K., Effect of porosity and grain size on the microwave dielectric properties of sintered alumina, J. Am. Ceram. Soc. 80 (7) (1997) 1885–1888.

[9] Roussy G., Bennani A., Thiébaut J.M., Temperature runaway of microwave irradiated materials, J. Appl. Phys. 62 (4) (1987) 1167–1170.

[10] Spotz M.S., Skamser D.J., Johnson D.L., Thermal stability of ceramic materials in microwave heating, J. Am. Ceram. Soc. 78 (4) (1995) 1041–1048.

[11] Thomas J.R., Particle size effect in microwave-enhanced catalysis, Catal. Let. 49 (1997) 137–141.

[12] Tinga W.R, Fundamentals of microwave–material interactions and sintering, in: Sutton W.H. (Ed.), Mat. Res. Soc. Symp. Proc., Vol. 124, Microwave Processing of Materials, 1988, pp. 33–43.

[13] Chatterjee A., Basak T., Ayappa K.G., Analysis of microwave sintering of ceramics, AIChE J. 44 (10) (1998) 2302–2311.

[14] Sutton W.H., Microwave processing of ceramic materials, Am. Ceram. Soc. Bull. 68 (2) (1989) 376–386.

[15] Westphal W.B., Sils A., Dielectric constant and loss data, Technical Report AFML-TR-72–39, Air Force Material Laboratory, Wright-Patterson Air Force Base, OH, USA, 1972.

[16] Hutcheon R.M., De Jong M.S., Adams F.P., Lucuta P.G., McGregor J.E., Bahen L., RF and microwave dielectric mesurements to 1 400 °C and dielectric loss mechanisms, in: Mat. Res. Soc. Symp. Proc., Vol. 269, 1992, p. 541.

[17] Booske J.H., Cooper R.F., Freeman S.A., Microwave enhanced reaction kinetics in ceramics, Mat. Res. Innov. 1 (1997) 77–84.

[18] Vriezinga C.A., Thermal runaway in microwave heated isothermal slabs, cylinders and spheres, J. Appl. Phys. 83 (1) (1998) 438–442.

[19] Ferrière A., Philippot E., Méthode de résolution par différences finies de l'équation de la chaleur en géométrie bidirectionnelle cylindrique anisotrope, IMP-CNRS Internal Report, February 1994.